33RD CONGRESS
OF THE INTERNATIONAL COUNCIL
OF THE AERONAUTICAL SCIENCES
STOCKHOLM, SWEDEN, 4-9 SEPTEMBER, 2022

ICAS 2022 SWEDEN

A COMPARITIVE ASSESSMENT OF MULTI-OBJECTIVE OPTIMISATION METHODOLOGIES FOR AERO-ENGINE NACELLES

Avery Swarthout[1], David MacManus[1], Fernando Tejero[1], Jesús Matesanz-García[1], Luca Boscagli[1]& Christopher Sheaf[2]

[1]Centre for Propulsion Engineering, School of Aerospace, Transport and Manufacturing, Cranfield University, UK
[2]Rolls Royce Plc., Derby, UK

Abstract

There are significant environmental and economic drivers for the development of more fuel-efficient commercial aircraft engines. The propulsive efficiency benefits of ultra-high bypass ratio turbofans may be counteracted by the drag and weight penalty associated with larger nacelles. A more compact nacelle design may therefore be necessary to reduce these penalties. However, increasing compactness also increases the sensitivity of the nacelle to boundary layer separation under off-design windmilling conditions. This paper investigates methods for incorporating windmilling considerations alongside design point requirements within a multi-objective, multi-point optimisation. Windmilling under aircraft diversion and at the end-of-runway (EoR) condition are considered. The windmilling conditions are assessed through a combination of regression and classification type criteria. The transonic aerodynamics of the nacelle at the design point are notably different from the transonic characteristics at the diversion windmilling conditions. Meanwhile, the aerodynamics, and separation mechanisms, at the end-of-runway condition are dominated by subsonic diffusion. Overall, a combination of regression and classification mechanisms are found to be most suitable for the nacelle optimization as it delivers a design population which is favorably balanced between robustness against boundary layer separation as well as delivering nacelle drag benefits.

Keywords: Nacelle, Optimisation, CFD, Off-Design, Separation

1. Introduction

For turbofans, the requirement for higher propulsive efficiency and reduced specific fuel consumption (SFC) typically drives the powerplant system design to higher bypass ratios, larger fan diameters, and lower fan specific thrust [1]. However, the cycle benefits may be reduced by the drag and weight penalties associated with larger nacelles. One way to mitigate this could be the development of more compact nacelle designs [2]. This increase in compactness is likely to make the nacelle more sensitive to off-design conditions such as windmilling when one engine is not operating [3]. Under free-windmilling conditions, the fan rotates at a low speed under the ram pressure of the intake flow [4]. The engine mass flow capture ratio (MFCR) reduces significantly which causes high levels of flow spillage [3]. Compact nacelles designed with legacy methods that typically optimise around the cruise segment may not have an acceptable performance at these off-design conditions. Therefore, it is necessary to consider windmilling scenarios from an early stage in the design process. Such an optimisation is multi-point and multi-objective by nature because the requirements for cruise and off-design performance present a significant conflict [5].

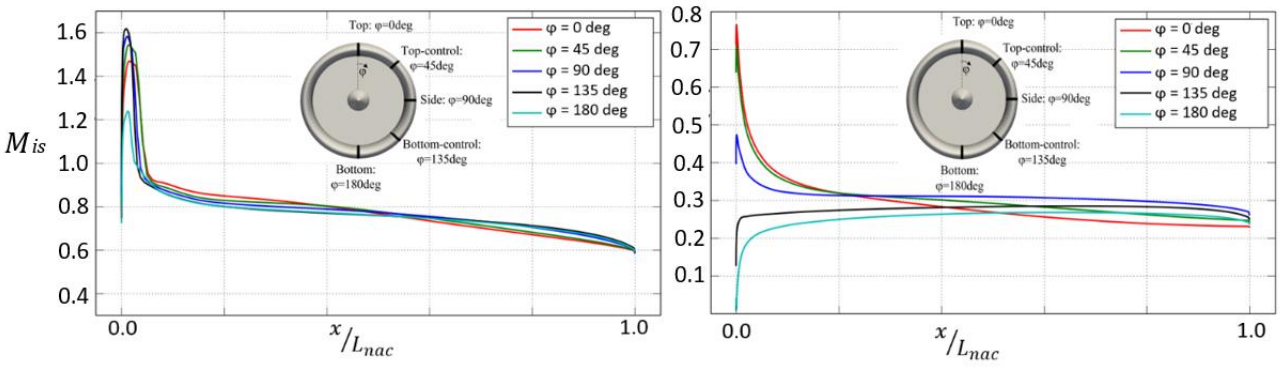

Figure 1 – The isentropic Mach Number distribution around a typical compact nacelle azimuth under diversion windmilling conditions. (M = 0.65, AoA = 4.5 deg) (Left), and End of Runway windmilling (M = 0.25, AoA = 20.0 deg) (Right).

This paper presents a methodology to incorporate windmilling conditions into a multi-objective optimisation (MOO) problem. Two scenarios for windmilling are considered in this work: diversion and end-of-runway (EoR). During aircraft diversion conditions, the flow spillage for the windmilling engine can result in high peak Mach numbers and a shock close to the leading edge of the nacelle (Figure 1). Separated flow may develop due to the shock boundary layer interaction which typically reattaches further downstream (Figure 2). Overall, there is a notable increase in the nacelle drag in the order of 30-50%. Windmilling at the end-of-runway is dominated by a high angle of attack and relatively low Mach numbers. The incidence onto the nacelle at EoR windmilling conditions is typically around 20 degrees [6]. Under these conditions the spillage around the highlight and nacelle lip results in a substantial adverse pressure gradient over the nacelle aft body which may induce large regions boundary layer separation (Figure 2). Under cruise conditions, the nacelle aerodynamics are typically characterised by an almost isentropic acceleration up to the nacelle crown followed by a normal shock with no separation [7]. These two windmilling conditions are therefore dominated by aerodynamic phenomena which are considerably different from the flow field under cruise conditions. Consequently, this increases the complexity of the MOO process to take both cruise and windmilling off-design conditions into account [8].

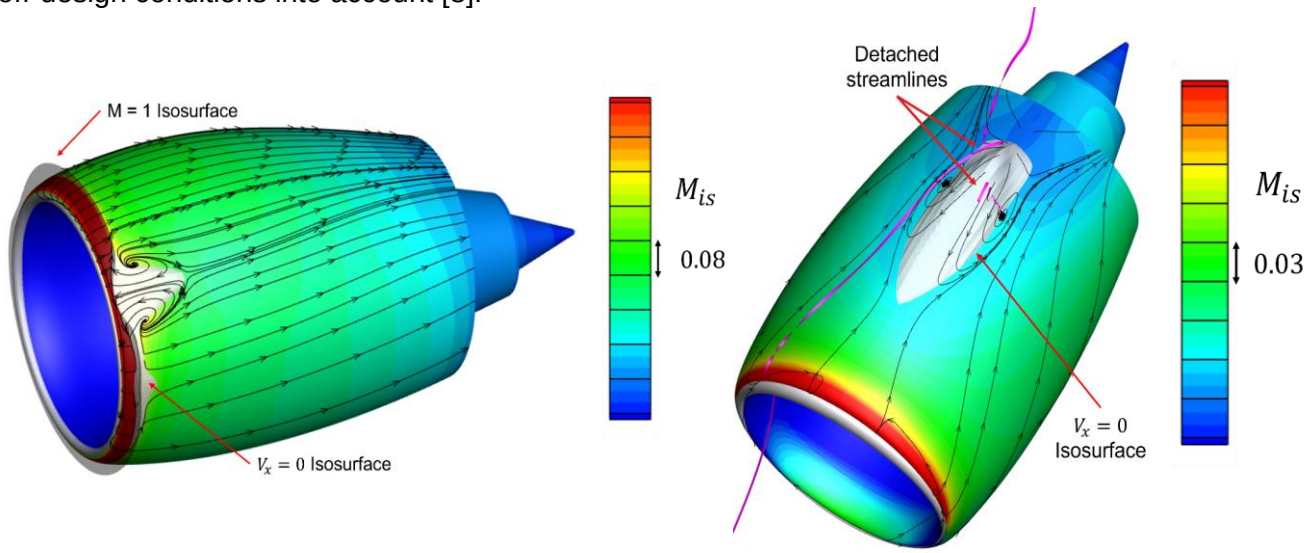

Figure 2 – Surface streaklines and isentropic Mach number contours for a compact nacelle with separated flow under diversion windmilling conditions (M=0.65, AoA=4.5) (Left) and EoR windmilling (M=0.25, AoA=20.0) (Right).

2. Methodology

2.1 Multi-Objective Optimisation

The 3D compact nacelle geometry was defined using 5 control aerolines with X-Z orthogonal symmetry (Figure 3). Each aeroline was constructed from an intuitive class shape transformation (iCST) curve [9]. The bulk dimensions of the nacelle such as length (L_{nac}/r_{hi}), highlight radius, scarf and droop were held constant (Figure 3). Each control aeroline was parameterised with 4 degrees of freedom ($lfore$, $rmax$, rif, βnac) to yield a 20 degree of freedom optimisation problem (Figure 3) [9]. Four operating conditions were considered within the optimisation problem, 2 for cruise and 2 for windmilling (Table 1). The 2 conditions considered for the cruise phase of the flight were one at the nominal mid-cruise point (M=0.85, MFCR~0.7), and one at a slightly increased Mach number (M=0.87, MFCR~0.7) to evaluate the wave drag sensitivity of the designs [10].

The optimisation method applied a CFD-in-the-loop process that was initialised from a Latin hypercube sampling (LHS) of 400 individuals for the initial design space exploration. A solution is computed for every design at each operating condition with a steady Favre Averaged Navier Stokes (RANS) calculation. The mesh used for the RANS calculation has approximately $1x10^6$ hexahedral, structured elements for each geometry and is constructed for a target y+ of 30-50 [2]. The kw-SST turbulence model is used for all calculations.

Operating Conditions for the 3D MOO			
	Mach Number	MFCR	Angle of Attack (deg)
Mid Cruise	0.85	~0.700	4.5
Increased Mach Number	0.87	~0.700	4.5
Diversion Windmilling	0.65	<0.500	4.5
End of Runway Windmilling	0.25	<0.500	20.0

Table 1 – Operating conditions used within each optimisation.

Up to 19 subsequent generations of 150 individuals were required to reach converged solutions. Across the three optimisations, 7,450 designs were evaluated with more than 29,000 3D CFD solutions. Convergence of the optimisation process was assessed through a hypervolume index. When the relative change between the hypervolume index for each generation was less than 1%, the optimisation was considered converged. Three strategies have been tested to evaluate the best way to consider the windmilling scenarios (Table 1). For each of the three optimisation strategies, the two cruise conditions are optimised based with the particle swarm algorithm OMOPSO in a regressive approach to minimise the overall drag [12]. The windmilling conditions were considered either through the same regressive model as for the cruise conditions or, they were classified based on a threshold value of the length of separation over the nacelle surface. For Optimisation 1, windmilling conditions was only considered regressively to minimise drag (Table *2*). For Optimisation 2, the EoR and diversion windmilling conditions were classified based on a selected threshold of the boundary layer separation length of 5% of the total nacelle length. For diversion, any designs which failed this threshold were then filtered out of the optimisation. For Optimisation 3, both EoR and diversion windmilling conditions were assessed purely through classification. Each optimisation was initialised from the same LHS of the initial design space.

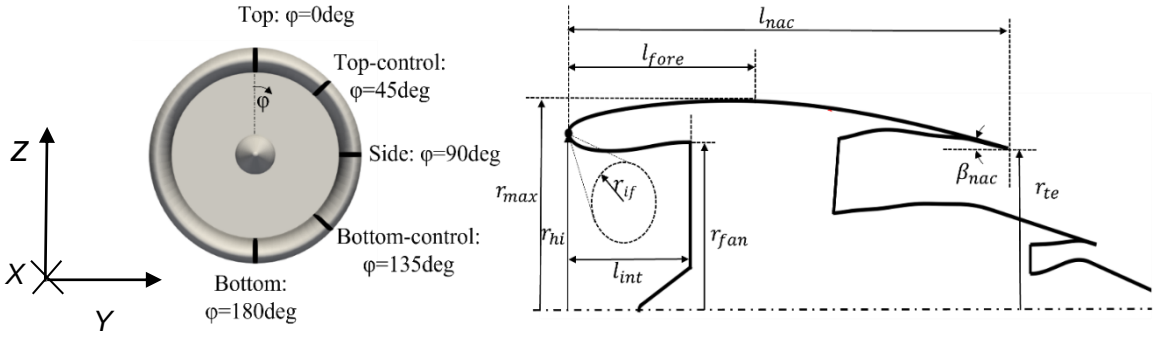

Figure 3 – Geometric parameterisation of the 5 aerolines (left) and the geometric parameters for each aeroline (right).

Windmilling Strategy for the 3D MOO			
	Optimisation 1	Optimisation 2	Optimisation 3
Mid Cruise	Regression, Min(Drag)	Regression, Min(Drag)	Regression, Min(Drag)
Increased Mach Number	Regression, Min(Drag)	Regression, Min(Drag)	Regression, Min(Drag)
Diversion Windmilling	Regression, Min(Drag)	Classification, $\frac{l_{sep}}{l_{nac}} < 0.05$ & Regression, Min(Drag)	Classification, $\frac{l_{sep}}{l_{nac}} < 0.05$
EoR Windmilling	Regression, Min(Drag)	Classification, $\frac{l_{sep}}{l_{nac}} < 0.05$	Classification, $\frac{l_{sep}}{l_{nac}} < 0.05$

Table 2 – Methodologies tested in each optimisation for assessing the compact nacelle performance at the operating conditions.

2.2 Down-Selection

The multi objective optimisation (MOO) returns a Pareto front of non-dominated designs which are optimum within the context of the specified constraints and objectives (Table 1)[2]. The Pareto front therefore needs to be searched in order to find a candidate design which can be evaluated in further detail [2]. This process, referred to as down selection, should therefore fulfil 2 main criteria:

- Identify designs which have minimum cruise drag and offer benefits at off design conditions relative to conventional nacelles [13].

- Identify flow fields which are expected to be robust against perturbations in on- and off-design operating conditions [14].

Although there is an empirical method of evaluating nacelle performance in terms of drag, classifying nacelle designs through similarities in their flow signatures (i.e., shockwaves) is not straightforward and often relies on the experience and intuition of the designer. Machine learning algorithms can assist in this process by grouping designs based on the relative similarities between their isentropic Mach number (M_{ise}) fields [15]. In this work, the k-means clustering algorithm has been applied (Figure 4). The k-means algorithm assembles nacelle designs into a predefined number of groups [16]. As this algorithm is distance based, it requires continuous value features [17]. However, it is useful to classify designs based on some discrete features such as the number and strength of shockwaves. Other flow features of interest are the peak isentropic Mach number or the amount of flow acceleration over the forebody are of interest as well [18]. Three features have been used to

cluster the designs based on the M_{ise} distributions along the 45-degree aeroline during mid-cruise [18]:

$$\sum_{x/L_{nac}=0}^{x/L_{nac}=1} (M_{ise}) \quad (1)$$

$$\sum_{x/L_{nac}=0}^{x/L_{nac}=1} \left(\left| \frac{d(M_{ise})}{dx} \right| \right) \quad (2)$$

$$\sum_{x/L_{nac}=0}^{x/L_{nac}=1} \left(\left| \frac{d^2(M_{ise})}{dx^2} \right| \right) \quad (3)$$

The features will highlight designs which have high peak Mach numbers, substantial changes in their Mach number gradient (i.e., through a shockwave) or large changes in concavity along the top control aero line (i.e., due to non-monotonic compression or oblique shocks) [20]. Within the k-means algorithm, the features have been scaled to create a more uniform space for the clustering [16]. The non-dominated group was first filtered to obtain the 40 lowest mid cruise drag designs. Different cluster counts were tested to establish how many families of designs each MOO had provided.

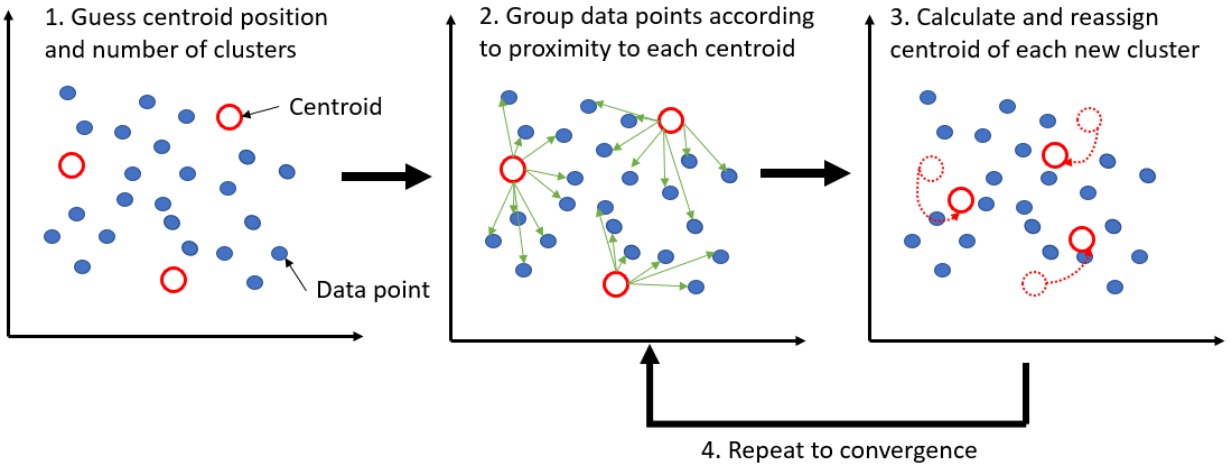

Figure 4 - Schematic diagram outlining the steps taken during each iteration of the k-means clustering algorithm.

Within the cluster which contains the minimum cruise drag for each optimisation, an individual was selected for which the increased Mach number and diversion drag were at most 25% greater than the individual's mid-cruise drag ($C_{d-midcruise}$) [12]. These downselected individuals were then analysed with more detailed RANS studies.

Case Matrix for Candidate Geometry Evaluations			
Condition	Mach Number	MFCR	AoA (deg)
Cruise	0.8 – 0.9	~ 0.7	4.5
Diversion Windmilling	0.65	<0.5	4.5
End of Runway Windmilling	0.25	<0.5	14 – 30

Table 3: Case matrix for sensitivity analysis against operating condition perturbations.

2.3 Detailed CFD Investigation

An aircraft's operating envelope may differ from the flight conditions prescribed in the MOO. There is also uncertainty regarding the turbofan cycle under windmilling [[21], [22]]. Therefore, the aerodynamics of candidate geometries from each optimisation have been assessed for a range of flight conditions (Table 3). Each candidate geometry has been discretized using a multi-block structured mesh of approximately $3.5x10^6$ elements for a target y+ < 1. Because the optimisations employ symmetry along the X-Z plane in the geometric parameterisation (Figure 3), the further CFD studies also employ a symmetry plane. The solver was an explicit, density-based method for all the solutions. For each candidate, 3 studies have been performed (Table 3). At cruise, CFD studies for a range of flight Mach numbers evaluate the sensitivity of wave drag penalties to changing flight conditions. Under diversion windmilling, the fundamental mechanism of separation is shock driven close to the leading edge. The impact of flow spillage on this separation was assessed for a range of MFCR. At the end of runway windmilling condition, the separation is onset through diffusive mechanisms. As this is at an end of runway condition, the effect of incidence was studied to evaluate the onset of separation at the windmilling MFCR.

3. Results of the Optimisation

3.1 Relative Optimisation Performance

Compared with optimization 1, the methods 2 and 3 require approximately twice as many generations to reach convergence (Figure 5). As each optimisation is initialised from the same LHS, Optimisations 2 and 3 are two times more computationally expensive compared with Optimisation 1. However, the Pareto front from Optimisation 1 was filtered based on a threshold that the separated flow length is not greater than 5% of the nacelle length. Then, only 43 designs remained in the non-dominated group out of the original 112. Additionally, the non-dominated designs from Optimisation 1 which failed the classification threshold were almost entirely within the lowest 10% of mid-cruise drag and the lowest 30% of diversion drag (Figure 6). Relative to before the filter was applied, the minimum cruise drag design after the filter had a 6.5% mid-cruise penalty. Method 1 did not obtain optimum designs within the 5% separation threshold because designs with larger separations were not excluded from the optimisation.

By contrast, Optimisation 2 found 82 Pareto individuals that all passed the classification threshold based on the separation length. The consequence of this is that the minimum cruise drag achieved for an acceptable design from Optimisation 2 was 3.6% lower that the best designs from Optimisation 1 which were filtered a posteriori to meet the separation criteria. Optimisation 2 has a more restricted space within the final Pareto front but twice as many acceptable designs (Figure 7). Therefore, Optimisation 2 balances the increase in computational cost with a diverse population of optimum designs across the entire performance range of the compact nacelle.

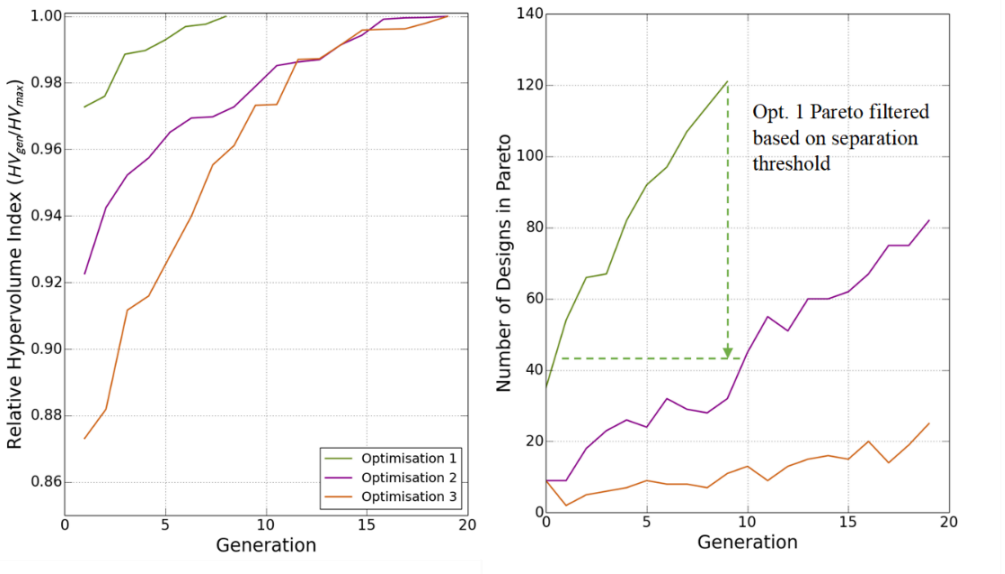

Figure 5 – Relative hypervolume index for each of the 3 optimisations (left) compared against the number of non-dominated individuals over each generation (right).

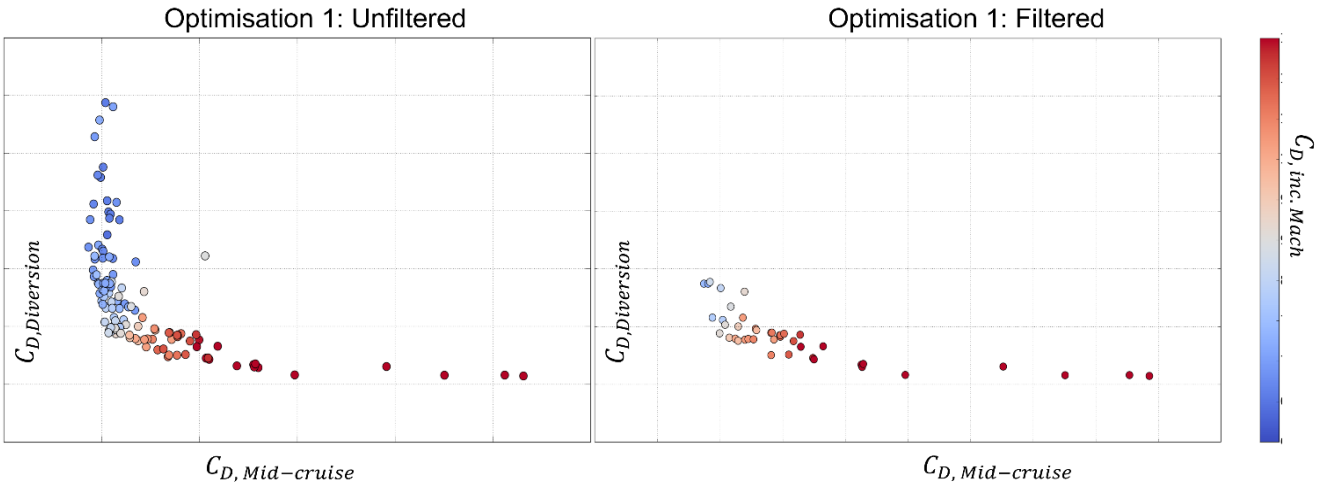

Figure 6 – Optimisation 1 Pareto front before the designs were filtered based on the separation threshold ($\frac{l_{sep}}{l_{nac}} < 0.05$) (left) and after the filtering (right).

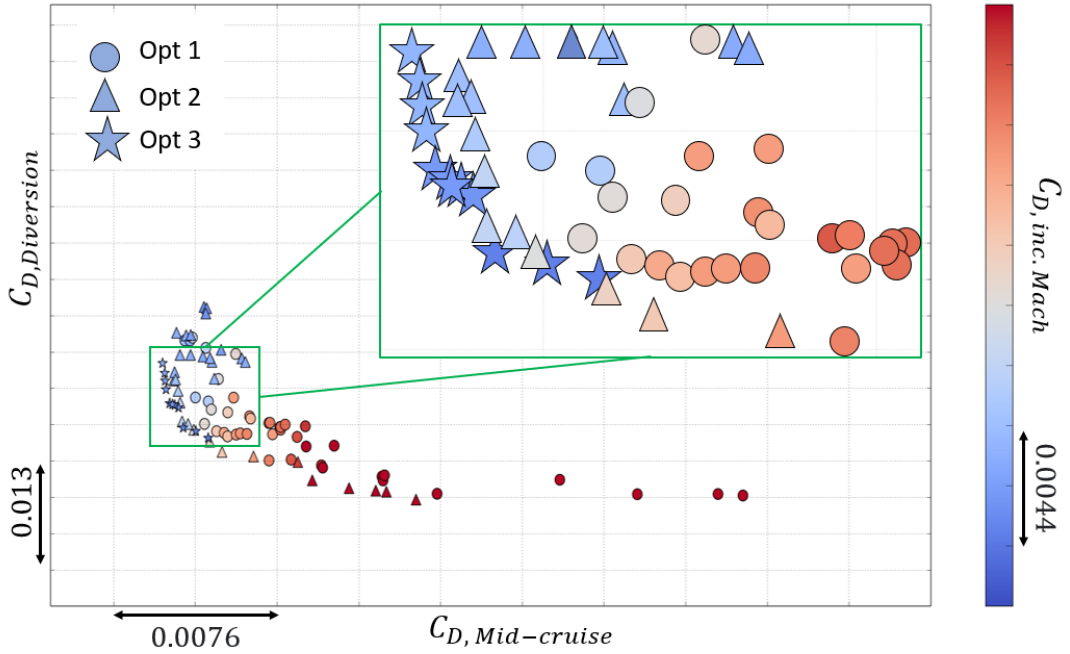

Figure 7 – Final Pareto fronts for each of the three optimisations superimposed upon each other.

Results of 3D MOO			
	Optimisation 1 (Reference)	Optimisation 2	Optimisation 3
Number of Overall Designs	112	82	25
Number of Acceptable Designs	43	82	25
Number of Generations	9	19	19
Relative Computational Cost	1.0	2.0	2.0
Minimum Mid-Cruise C_d (Relative to Opt. 1)	Reference	-3.6%	-5.9%
Diversion C_d for best Mid-Cruise Design (Relative to Opt. 1)	Reference	-4.0%	+5.0%

Table 4 – Results detailing the performance of each optimisation in terms of Pareto population size, computational cost and drag.

Optimisation 3 has the most restrictive conditions with 2 classification-based functions at windmilling and 2 regressive objective functions at cruise (Table *2*). It only identified 25 final non-dominated individuals whereas Optimisations 1 and 2 identified 112 and 82 individuals, respectively. This is because the classification model restricts the diversity of the design space used to generate each subsequent iteration. The design space exploration (generation 0) populated the non-dominated group with 40 individuals for Optimisation 1 but less than 10 individuals for Optimisations 2 and 3. This explains the increase in convergence time and computational cost for the classification model in

the latter optimisations (Figure 5). Conversely, 75% of the initial designs passed into the Optimisation 1 non-dominated group did not have acceptable windmilling flow characteristics based on the separation length threshold. The converged Pareto set had 70% fewer non-dominated designs compared with Optimisation 2. Overall, compared with Optimisation 2, Optimisation 3 provided a design with a 2.3% lower mid cruise drag but 9% higher diversion drag (Table 4). Despite the mid-cruise drag benefit for Optimisation 3, the highly restricted Pareto front and large windmilling drag penalty may render this approach unsuitable for practical design applications. Overall, it is concluded that the classification/regressive hybrid model for diversion windmilling (Optimisation 2) maintains diversity within the non-dominated population, provides a reduction in the nacelle cruise drag, but can also successfully meet additional, user-specified classification requirements based on the length of the boundary layer separation at off design condition.

3.2 Pareto Front Design Space Comparison

3.2.1 Geometric Degrees of Freedom

The geometric trends of the optimal design space were assessed for each of the three optimisations (Figure 8). There are some notable differences in the trends which indicate how the different assessment of windmilling conditions affects the final design space. Across all 20 degrees of freedom, optimisation 1 (filtered) has the widest variation in its geometric parameters for each aeroline. Clearly, the lack of a classification model for this approach permits the particle swarm algorithm to minimise the drag of each objective function without any exclusion criteria and yields an overall wider space of optimum individuals. Conversely, optimisation 3 has the narrowest design space as only the 2 cruise functions are handled by the regressive drag minimisation function. By extension, the range in degrees of freedom for optimisation 3 are generally narrower when compared with the other 2 approaches. Furthermore, there exist certain degrees of freedom for which optimisation 3 drives to a completely different part of the final design space. For instance, the top-line forebody length for optimum designs is notably larger for optimisation 3 compared against optimisations 2 and 1. Similarly on the top line, the final boat tail angle is about 1 degree higher for optimisation 3 compared against optimisation 2. This may indicate that the classification model is over-restricting the final design space. Overall, the value of parameters to describe the top line geometry are substantially higher between optimisation 3 and the others. This indicates the nacelle top line for optimisation 3 will have a shorter forebody and larger maximum radius. The curvature of this aeroline will be stronger to accommodate these degrees of freedom within the iCST. In order to then achieve a minimum cruise, drag, the maximum radius on the other aerolines for optimisation 3 is lower indicating a slimmer geometry as one moves around the nacelle azimuth.

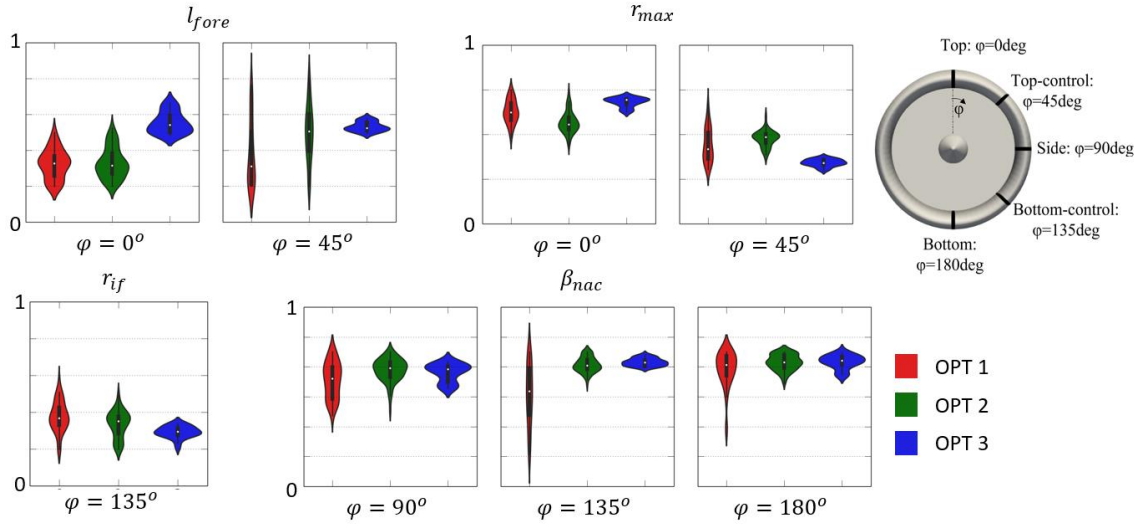

Figure 8 – Violin plots for geometric degrees of freedom compared across the 3 MOOs.

The bottom 3 aerolines (φ = 90, φ = 135, and φ = 180) show a clear story across the three optimisations. The design space is overall the widest for the filtered optimisation 1 and converges progressively as classification is added for optimisations 2 and 3. This shows how the classification models restrict parts of the design space which may lead to infeasible windmilling performance during the optimisation. It therefore allows the algorithm to achieve a better minimum cruise drag design for a given level of windmilling separation.

A comparison between the effect of the different optimisations on the top control line (φ = 45) indicates 2 main points. First, this aeroline contributes significantly to the diversion windmilling performance of the compact nacelle. There are significant differences in both the range of parameters as well as the median value between the 3 optimisations. Furthermore, in conjunction with Table *4*, the hybrid model used for diversion windmilling within optimisation 2 limits the design space to regions of acceptable flow separation while maintaining sufficient diversity of the final population to yield low drag designs for this operating condition. Optimisation 3, which clearly has a more restrictive final design space for the 45-degree aeroline, also has a 10% higher diversion drag compared with optimisation 2.

3.2.2 Clustering and Down Selection

For each of the optimisations, the clustering and down selection process was followed. Given that the datasets are comparatively small, only the 45-degree aerolines for each design at the mid cruise conditions (M=0.85, AoA = 4.5) are compared (Figure *9*). The 45-degree aeroline gives rise to the most diverse set of flow physics across the design space [8]. Each optimisation found a different number of design families using this clustering approach. For optimisation 1, the algorithm identified 4 clusters. Clusters 1 and 3 are the most populated. Both clusters include designs with considerable acceleration over the nacelle lip and highlight compared with clusters 2 and 4. This acceleration over the lip will generate a suction that reduces the mid-cruise drag [10]. For Cluster 1, the designs demonstrate a pre-shock compression that causes a local reduction in the isentropic Mach number between 0.05 and 0.1. For Cluster 3, there is a pre-shock compression which reduces the local Mach number by about 0.2. However, both clusters show acceleration ahead of the shock whereby the pre-shock Mach number recovers by 0.2. Hence, the pre shock Mach number for cluster 3 is 0.1 – 0.15 lower than for cluster 1.

Optimisation Number	Nacelle Name	Mid Cruise Drag	Increased Mach number Drag	Diversion Windmilling Drag
1	A1	Reference	Reference	Reference
2	A2	-4.0%	-2.9%	-2.0%
3	A3	-7.0%	-3.0%	+3.4%

Table 5 – The drag across various operating conditions for the downselected candidate from each optimisation.

The k-means algorithm identified 5 overall clusters for optimisation 2. However, it can be argued that clusters 1 and 3 may contain the same family of M_{ise} distributions. All clusters except for cluster 4 show the same characteristic acceleration over the lip. Therefore, incorporating the classification model for the diversion and end of runway windmilling conditions allows the optimizer to pursue designs which have more highly optimised M_{ise} distributions at design point conditions. Cluster 4 has much less initial acceleration compared with the other geometries. This type of design prevents very high Mach numbers from arising during diversion windmilling and is a result of the hybrid regression/classification function used for this operating point within the optimisation.

The M_{ise} distributions for each cluster from Optimisation 3 are the most well converged. This may be because there were only 25 samples to analyze from this optimisation which were in a comparatively narrow region of the Pareto front. Clusters 2 and 4 comprise essentially the same family of designs

which are characterised by a double shock topology on the 45-degree aeroline. Clusters 1 and 3 have a compression wave followed by a normal shock. All the designs in Optimisation 3 have similar loadings of the Mis distribution on the nacelle forebody. Optimisation 3 had no regressive functions applied to the windmilling operating conditions. Therefore, these flow fields are solely driven by minimizing the cruise drag.

Overall, the minimum cruise drag designs for Optimisations 1 and 2 were in cluster 1. For Optimisation 3, the minimum cruise drag design fell in cluster 3. For these three clusters across the optimisations, the minimum cruise drag design was selected for further analysis provided that the drag at increased Mach number and diversion windmilling conditions was not more the 25% larger than the mid-cruise drag (Table *5*). To evaluate the impact of different flight conditions and powerplant performance settings, each candidate was analysed using RANS CFD with boundary layer resolved mesh. The drag and windmilling flow separation mechanisms were then compared for each candidate.

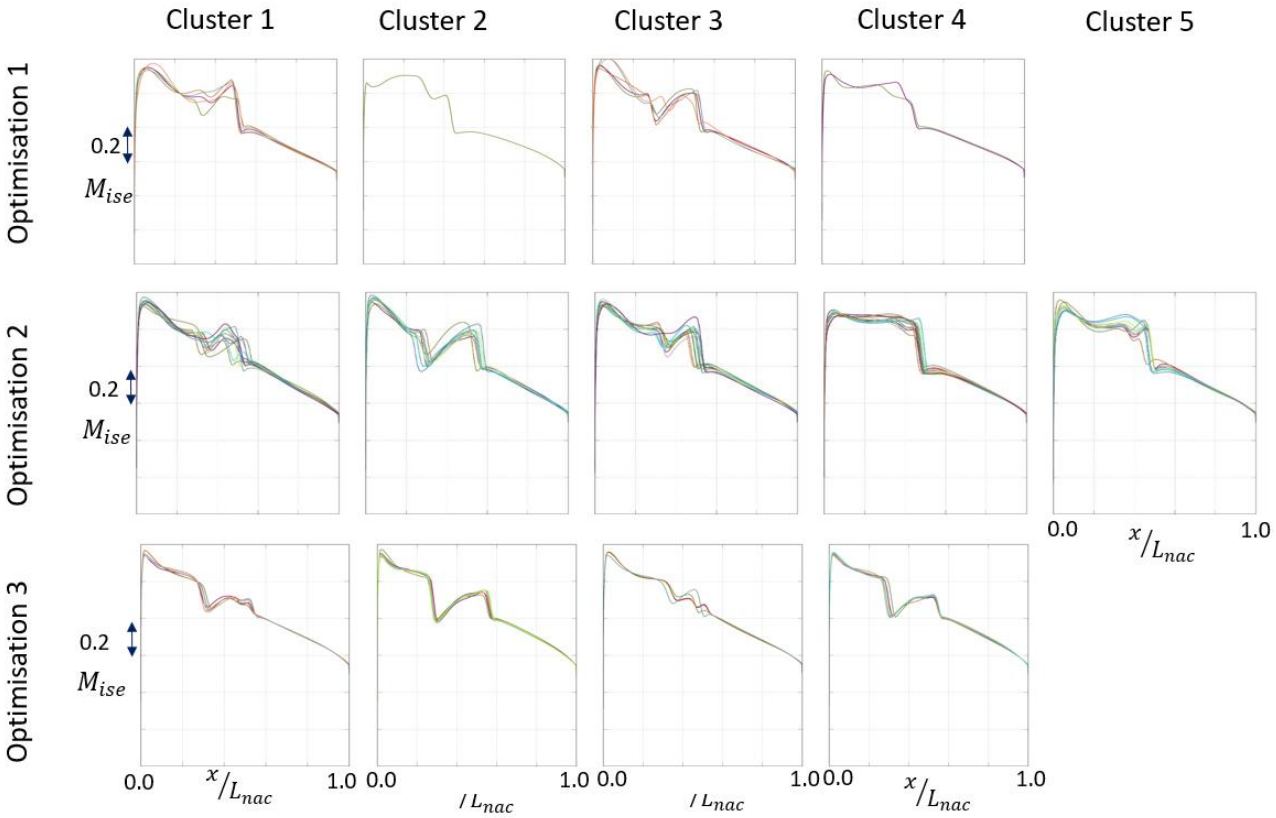

Figure 9 – Results of the k-means Clustering algorithm for the 45-degree aeroline of each nacelle at mid-cruise conditions (M=0.85, AoA=4.5 deg).

4. Aerodynamics of Optimised Nacelles

4.1 Cruise Conditions

The sensitivity of the nacelle drag to the flight Mach number was assessed for the three candidate design (Figure 10). Overall, the 3 designs demonstrate similar drag rise associated with increasing Mach number up to M= 0.87. A1 demonstrates a 30% larger increase in drag as the Mach number rises from 0.87 to 0.9 relative to A2. The 2 objective functions for cruise type conditions were handled in the same way across the three optimisations. These results indicate that incorporation of threshold classifiers for windmilling flows does not affect the sensitivity of the nacelle designs to wave drag penalties associated with high free stream Mach numbers. The shock structure at the nominal mid

cruise condition (M=0.85, AoA=4.5) provides further detail into the flow physics for each nacelle (Figure 11). All the designs have a shock signature on the top dead center position which is located at 45-50% of the nacelle chord. However, design A1 demonstrates a double shockwave which forms just aft of the nacelle crest whereas the other 2 optimisations have singular shockwaves located slightly further upstream, directly on top of the crest. for the latter 2 designs, there is no shock present on the bottom line. For all three nacelles, the shockwave moves upstream by about 10% of the nacelle chord between the top dead center and bottom dead center positions. Overall, the shock structure and cruise performance is similar across the down selected nacelles.

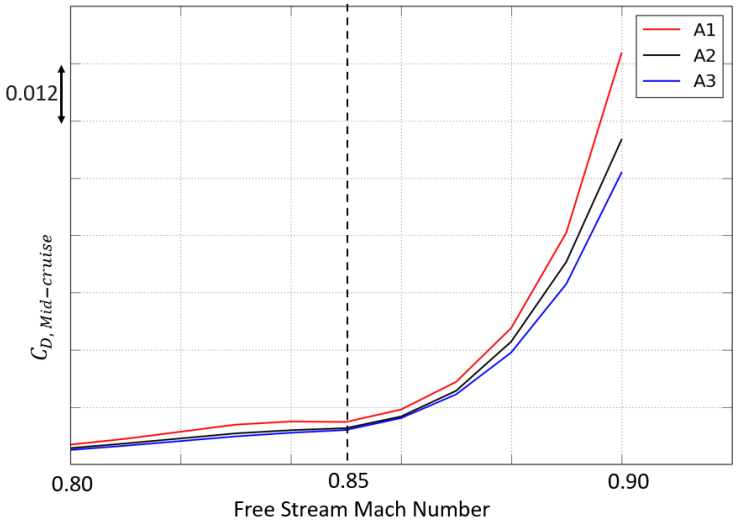

Figure 10 - Variation of the drag coefficient with free stream Mach number at mid cruise conditions.

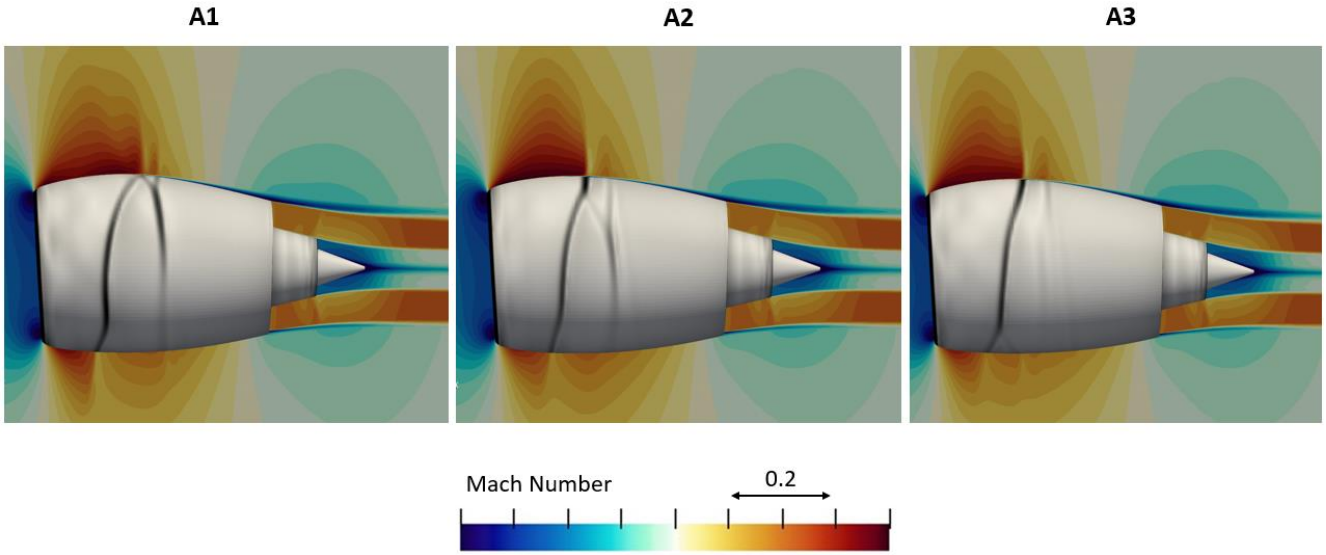

Figure 11 - Symmetry plane Mach number contours and nacelle surface streamwise density gradients (dρ/dx) for each candidate nacelle at the nominal mid-cruise condition (M=0.85, AoA=4.5).

4.2 Diversion Windmilling

CFD for a range of mass flow capture ratio (MFCR) has been conducted at diversion windmilling conditions for each nacelle. The objective is to determine the onset of boundary layer separation and then compare the mechanism of this separation for each design. The strongest shock waves and by extent, the onset of the shock driven separation arises on the φ=45-degree aeroline. The results of the MFCR study show that design A2 is the most robust in that separation is only onset from MFCRs below the requirement specified in the optimisation (Figure 12). Relative to A2, A1 separates at 0.1 higher MFCR. This is expected as the optimisation to obtain A1 did not make any considerations as to flow separation prevention. Interestingly, A3 is the design with the earliest separation onset between 0.05 and 0.1 above the design point MFCR from the MOO. The optimisation for A3 only considered windmilling conditions through a threshold classifier on the amount of flow separation.

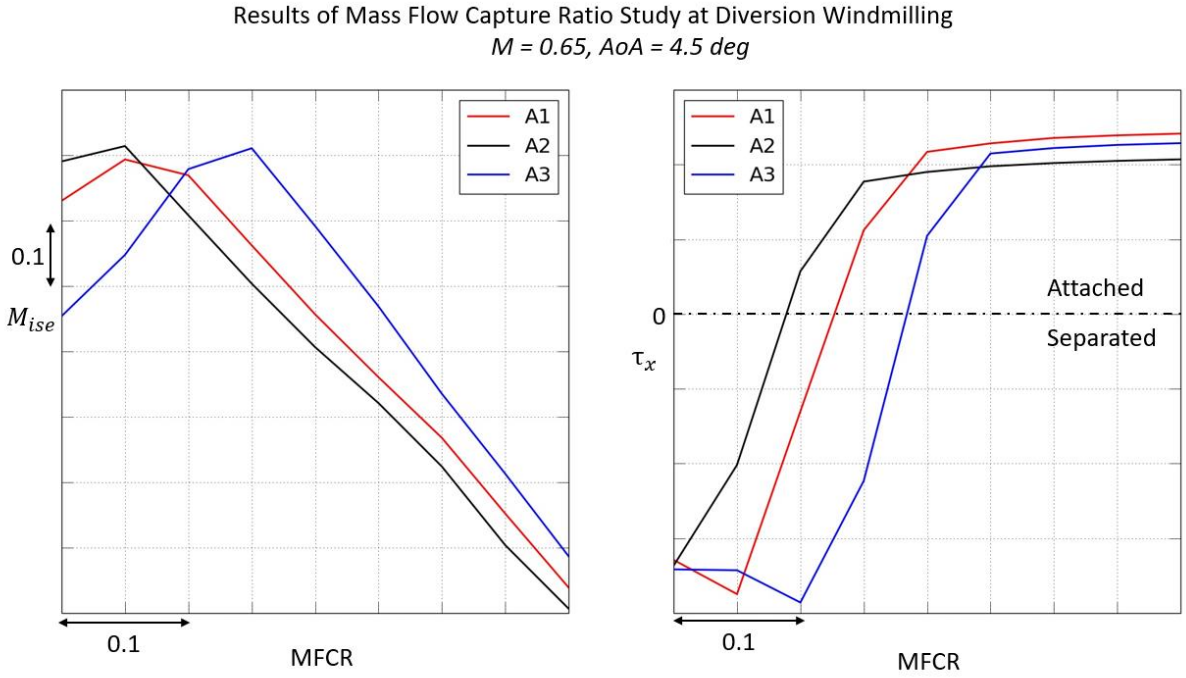

Figure 12 – Maximum isentropic Mach number (left) and minimum x wall shear stress (right) plotted for each nacelle against changing MFCR at the 45-degree aeroline during aircraft diversion (M=0.65, AoA=4.5)

Overall, the mechanism of flow separation is shock driven at the leading edge and typically initiated at the 45-degree aeroline (Figure 13). Despite subtle differences between the 3 candidates, they all undergo the same shock driven mechanism and experience growth of the separation in the same way. At higher mass flow capture ratios, the presence of the leading-edge shock does not induce any boundary layer separation. As the mass flow capture ratio is reduced, separation is initiated in a quasi-2-dimensional manner and remains highly localized around the nacelle leading edge. At this point, the length of the separation may only be 2-4% of the total nacelle length. Further reduction of the mass flow capture ratio generates 3 dimensionality in the separated region. The separation does also grow in the streamwise direction by a factor of 3-4. When the separated region becomes large enough, it will extend all the way to the leading edge.

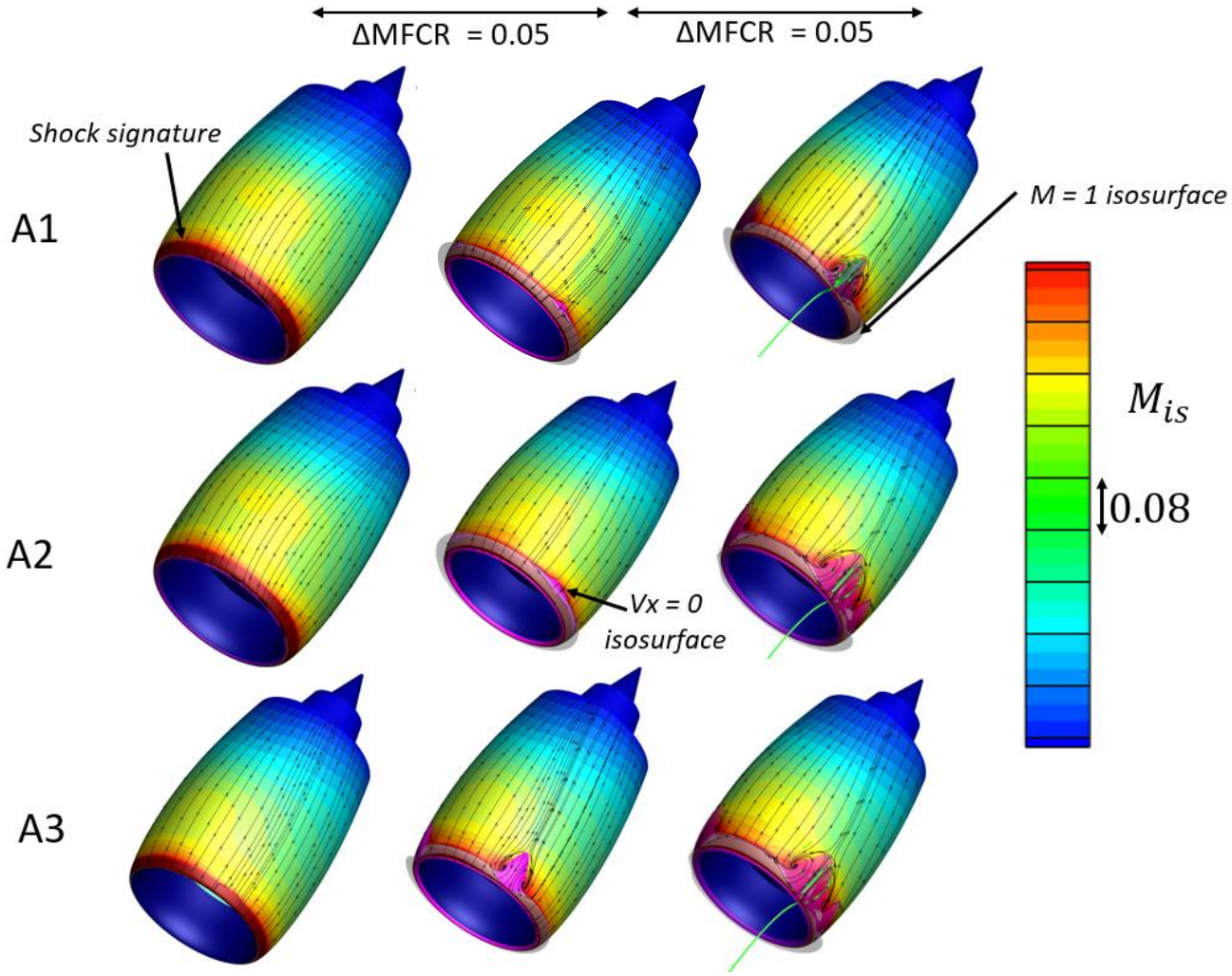

Figure 13 – Nacelle surface isentropic Mach number contours for each candidate nacelle across a range of mass flow capture ratios to show how the separation develops for each nacelle.

4.3 End of Runway Windmilling

The diffusive separation mechanism at end of runway windmilling has been interrogated under a range of incidences from 14 to 30 degrees. The onset and growth of flow separation at these types of operating conditions was also compared. The peak isentropic Mach number for each design increases approximately linearly with incidence until the region of separated flow reaches the leading edge of the nacelle (Figure 14). Due to the fully developed separation at 30 degrees for each design leads to a reduction of the peak isentropic Mach number on the order of 0.07 to 0.1. Each candidate nacelle across the three optimisations has a critical incidence that is 7 degrees higher compared with the requirement proscribed in the multi objective optimisation (Table 1). Although design A2 is to be attached at 27 degrees it is right on the boundary between separated and attached (Figure *15*).

The mechanism of separation is subsonic and driven by the diffusion over the nacelle aft body at high incidence. There are no regions of supersonic flow. A small bubble of separation initiates at about 75% of the nacelle chord for each geometry at the critical incidence. As the angle of attack is increased, this region will grow steadily upstream to the nacelle crown. Up to this point the separation grows under an adverse pressure gradient. However, as the incidence for each candidate is increased from 29 to 30 degrees, the separated region breaches the nacelle crown and is sucked rapidly towards the leading edge by suction generated over the nacelle lip and highlight.

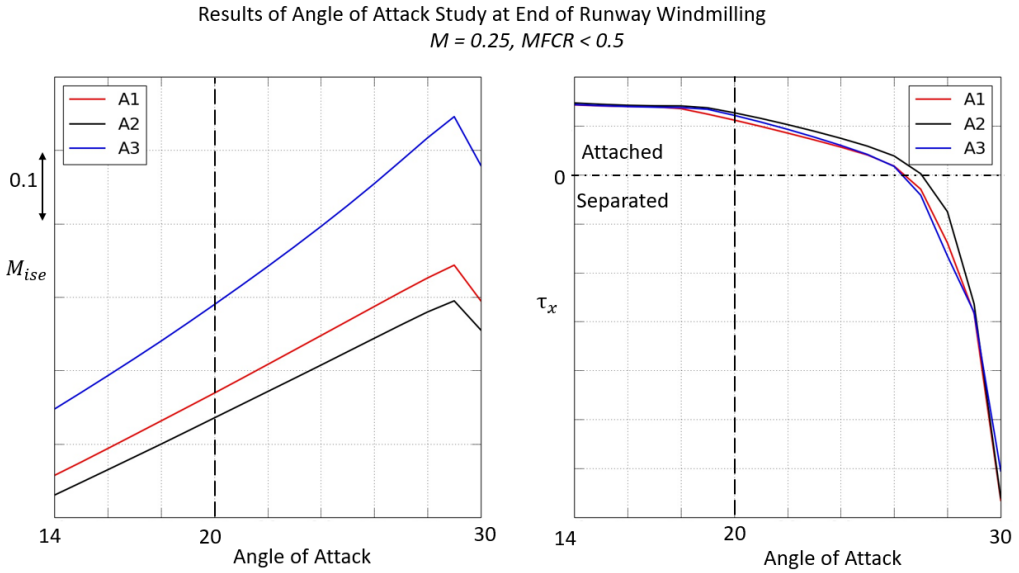

Figure 14 – Maximum isentropic Mach number (Left) and minimum x wall shear stress plotted for each nacelle against changing MFCR at the 0-degree aeroline during aircraft end of runway windmilling (M=0.25).

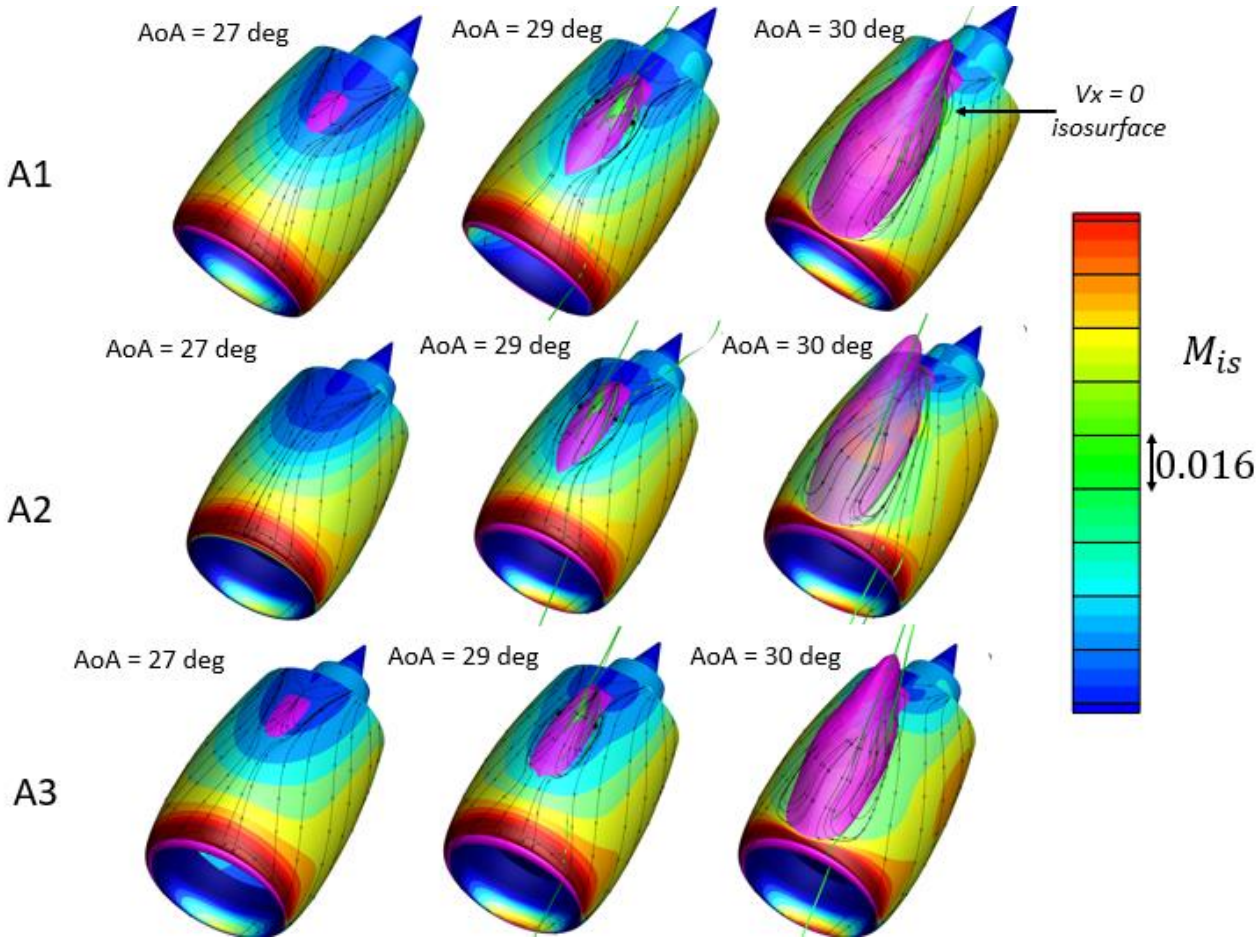

Figure 15 – Nacelle surface isentropic Mach number contours for each candidate nacelle across a range of angles of attack to show how the separation develops for each nacelle at end of runway windmilling (M=0.25).

5. Conclusion

This paper has tested 3 methods for aerodynamic multi-objective optimisations when the objective functions address different aspects of the flow physics. The method, which is based on a hybrid regression and classification model, is most suited to this problem and delivered a final design space that balances both low drag at the design point conditions and robust performance under off design conditions. The incorporation of the hybrid regression/classification model for diversion windmilling allowed the optimizer to find designs which did not experience separation under windmilling while maintaining a diverse Pareto population compared with the other 2 approaches. This represents an improvement on previous cowl design methods which use empirical judgement to assess whether a design will meet its off-design requirements at an early stage in the design process. A method of sorting and identifying designs based on the design point flow fields has also been presented. This provided a systematic manner of interrogating the design space based on both drag and intuitive knowledge of aerodynamic sensitivities to changes in operating conditions. As more compact powerplant installations are pursued, these design guidelines may no longer be valid. Therefore, it is important to have a method to incorporate off design performance requirements into an early stage of the development process. The proposed multi-point, multi-objective optimisation method is a significant initial step towards the development of an adequate design approach for compact aero-engine nacelles. In the future, the derived guidelines from this study will be incorporated into an optimisation that accounts for installation effects such as wing-pylon-nacelle interaction and the gully flow between the nacelle and aircraft fuselage.

6. Acknowledgements

This project has received funding from the Clean Sky 2 Joint Undertaking (JU) under grant agreement number 101007598. The JU receives support from the European Union's Horizon 2020 research and innovation programme and the Clean Sky 2 JU members other than the Union.

7. Copyright Statement

References

[1] N. Birch, 2020 Vision: The Prospects for Large Civil Aircraft Propulsion, The Aeronautical Journal vol. 104, no. 1038, pp 347-352, 2000

[2] Tejero, F., MacManus, D., Matesanz-Garcia, J., Swarthout, A., and Sheaf, C., 2022, "Towards the Design and Optimisation of Future Compact Aero-Engines: Intake/Fancowl Trade-off Investigation", Aero2022, 3AF, Toulouse.

[3] Schreiner, B., Tejero, F., MacManus, D., and Sheaf, C., 2020, "Robust Aerodynamic Design of Nacelles for Future Civil Aero-Engines", Volume 1: Aircraft Engine; Fans and Blowers.

[4] P. Zachos, "Modelling and Analysis of Turbofan Engines Under Windmilling Conditions", Journal of Propulsion and Power, vol. 29, no. 4, pp. 882-890, 2013. Available: 10.2514/1.b34729.

[5] S. Seraj and J. Martins, "Aerodynamic Shape Optimization of a Supersonic Transport Considering Low-Speed Stability", *AIAA SCITECH 2022 Forum*, 2022. Available: 10.2514/6.2022-2177.

[6] W. Hoelmer, J. Younghans and J. Raynal, "Effect of Reynolds number on upper cowl flow separation", *Journal of Aircraft*, vol. 24, no. 3, pp. 161-169, 1987. Available: 10.2514/3.45411.

[7] F. Tejero, D. MacManus and C. Sheaf, "Impact of Droop and Scarf on the Aerodynamic Performance of Compact Aero-Engine Nacelles", in AIAA Scitech 2020 Forum, Orlando, 2020.

[8] S. Qiu and X. Deng, "Multi-Point Design Optimisation of a High Bypass Ratio Fan Blade", in *Congress of the International Council of the Aeronautical Sciences*, Korea, 2016.

[9] F. Tejero, D. MacManus and C. Sheaf, "Surrogate-based aerodynamic optimisation of compact nacelle aero-engines", Aerospace Science and Technology, vol. 93, p. 105207, 2019. Available: 10.1016/j.ast.2019.05.059

[10] Tejero, F., MacManus, D., Hueso-Rebassa, J., Sanchez-Moreno, F., and Sheaf, C., 2022, "Aerodynamic Optimisation of Civil Aero-Engine Nacelles by Dimensionality Reduction and Multi-Fidelity Techniques", AERO2022, 3AF, Toulouse.

[11]I. Goulos, J. Otter, F. Tejero, J. Hueso Rebassa, D. MacManus and C. Sheaf, "Civil turbofan propulsion aerodynamics: Thrust-drag accounting and impact of engine installation position", *Aerospace Science and Technology*, vol. 111, p. 106533, 2021. Available: 10.1016/j.ast.2021.106533.

[12] F. Tejero, R. Christie, D. MacManus and C. Sheaf, "Non-axisymmetric aero-engine nacelle design by surrogate-based methods", *Aerospace Science and Technology*, vol. 117, p. 106890, 2021. Available: 10.1016/j.ast.2021.106890.

[13] S. Wang, G. Sun and C. Li, "Natural Laminar Flow Optimization of Transonic Nacelle Based on Differential Evolution Algorithm", *Journal of Aerospace Engineering*, vol. 32, no. 4, p. 06019001, 2019. Available: 10.1061/(asce)as.1943-5525.0001028.

[14] Y. Yao, D. Ma, M. Yang, L. Zhang and Y. Guo, "Adaptive-surrogate-based robust optimization of transonic natural laminar flow nacelle", *Chinese Journal of Aeronautics*, vol. 34, no. 10, pp. 36-52, 2021. Available: 10.1016/j.cja.2021.01.007.

[15] A. Afzal et al., "Response surface analysis, clustering, and random forest regression of pressure in suddenly expanded high-speed aerodynamic flows", *Aerospace Science and Technology*, vol. 107, p. 106318, 2020. Available: 10.1016/j.ast.2020.106318.

[16] Z. Zhang, "K-means Algorithm", https://user.engineering.uiowa.edu/~ie_155/Lecture/K-means.pdf, 2022.

[17] R. Meng and N. Xie, "A Competitive-Cooperative Game Method for Multi-Objective Optimization Design of a Horizontal Axis Wind Turbine Blade", *IEEE Access*, vol. 7, pp. 155748-155758, 2019. Available: 10.1109/access.2019.2949336.

[18] F. Tejero, I. Goulos, D. MacManus and C. Sheaf, "Effects of Aircraft Integration on Compact Nacelle Aerodynamics", *AIAA Scitech 2020 Forum*, 2020. Available: 10.2514/6.2020-2225.

[19] J. Sanwale and D. Singh, "Aerodynamic Parameters Estimation Using Radial Basis Function Neural Partial Differentiation Method", *Defence Science Journal*, vol. 68, no. 3, p. 241, 2018. Available: 10.14429/dsj.68.11843.

[20] S. Koziel, Y. Tesfahunegn and L. Leifsson, "Expedited constrained multi-objective aerodynamic shape optimization by means of physics-based surrogates", *Applied Mathematical Modelling*, vol. 40, no. 15-16, pp.

7204-7215, 2016. Available: 10.1016/j.apm.2016.03.020 .

[21] ESDU, "Estimation of Windmilling Drag and Airflow of Turbojet and Turbofan Engines", ESDU, 1984.

[22] N. García Rosa, A. Thacker and G. Dufour, "Periodic flow structures in a turbofan fan stage in windmilling", *Proceedings of the Institution of Mechanical Engineers, Part G: Journal of Aerospace Engineering*, vol. 235, no. 4, pp. 501-512, 2020. Available: 10.1177/0954410020948297.